

Article

# Oxygen-Ion and Proton Transport of Origin and Ca-Doped $\text{La}_2\text{ZnNdO}_{5.5}$ Materials

Ksenia Belova <sup>1,2</sup> , Anastasia Egorova <sup>1,2</sup>, Svetlana Pachina <sup>1</sup> , Irina Animitsa <sup>1,2</sup>  and Dmitry Medvedev <sup>1,2,\*</sup> 

<sup>1</sup> Institute of High Temperature Electrochemistry of the Ural Branch of the Russian Academy of Sciences, Akademicheskaya St. 20, 620066 Yekaterinburg, Russia; ksenia.belova@urfu.ru

<sup>2</sup> Institute of Hydrogen Energy, Ural Federal University, Mira St. 19, 620075 Yekaterinburg, Russia

\* Correspondence: dmitrymedv@mail.ru

**Abstract:** Oxygen-ionic and proton-conducting oxides are widely studied materials for their application in various electrochemical devices such as solid oxide fuel cells and electrolyzers. Rare earth oxides are known as a class of ionic conductors. In this paper,  $\text{La}_2\text{ZnNdO}_{5.5}$  and its Ca-doped derivatives  $\text{La}_2\text{Nd}_{0.9}\text{Ca}_{0.1}\text{ZnO}_{5.45}$  and  $\text{La}_2\text{ZnNd}_{0.9}\text{Ca}_{0.1}\text{O}_{5.45}$  were obtained by a solid-state reaction route. Phase composition, lattice parameters, and hydration capability were investigated by X-ray diffraction and thermogravimetric analyses. The conductivities of these materials were measured by the electrochemical impedance spectroscopy technique in dry ( $p\text{H}_2\text{O} = 3.5 \times 10^{-5}$  atm) and wet ( $p\text{H}_2\text{O} = 2 \times 10^{-2}$  atm) air. All phases crystallized in a trigonal symmetry with  $P3m1$  space group. The conductivity difference between undoped and calcium-doped samples is more than two orders of magnitude due to the appearance of oxygen vacancies during acceptor doping, which are responsible for a higher ionic conductivity. The  $\text{La}_2\text{Nd}_{0.9}\text{Ca}_{0.1}\text{ZnO}_{5.45}$  sample shows the highest conductivity of about  $10^{-3}$  S·cm<sup>-1</sup> at 650 °C. The Ca-doped phases are capable of reversible water uptake, confirming their proton-conducting nature.

**Keywords:** rare earth oxides; oxygen-ion conductivity; proton conductivity; hydrogen energy



**Citation:** Belova, K.; Egorova, A.; Pachina, S.; Animitsa, I.; Medvedev, D. Oxygen-Ion and Proton Transport of Origin and Ca-Doped  $\text{La}_2\text{ZnNdO}_{5.5}$  Materials. *Inorganics* **2023**, *11*, 196. <https://doi.org/10.3390/inorganics11050196>

Academic Editor: Chiara Dionigi

Received: 7 April 2023

Revised: 26 April 2023

Accepted: 27 April 2023

Published: 1 May 2023



**Copyright:** © 2023 by the authors. Licensee MDPI, Basel, Switzerland. This article is an open access article distributed under the terms and conditions of the Creative Commons Attribution (CC BY) license (<https://creativecommons.org/licenses/by/4.0/>).

## 1. Introduction

Oxygen-ionic and proton-conducting complex oxides are widely studied materials because of their potential application in various electrochemical devices such as solid oxide fuel cells and electrolyzers [1–9]. These devices allow hydrogen production from water (electrolyzers) and then convert this hydrogen directly into electrical energy (fuel cells) without any mechanical work. This type of energy conversion is therefore environmentally friendly and highly efficient compared to traditional energy sources [10–15]. The further development of hydrogen energy requires the development of new materials and devices based on them. Therefore, the search for new highly conductive electrolytic materials is very important. Traditional proton-conducting materials are complex oxides based on acceptor-doped barium cerates/zirconates [16–20]. This type of doping leads to the formation of oxygen vacancies in the anionic sublattice, which can be the reason for the increase in ionic conductivity in dry air and the formation of proton defects in the crystal structure in wet air.

Rare earth oxides have been the subject of proton conductivity studies by Norby et al. for about 30 years [21–25]. The effect of calcium as an impurity on the formation and value of proton transport of  $\text{La}_2\text{O}_3$ ,  $\text{Nd}_2\text{O}_3$ , and  $\text{LaNdO}_3$  oxides was investigated [26]. It was found that the oxides with more densely packed lattices and smaller cationic radii are characterized by a preference of proton transport as opposed to oxygen-ion transport. The  $\text{LaNdO}_3$  phase is therefore of interest from the viewpoint of the possibility of controlling the conductivity contributions and producing a material with the desired properties. However, studies of these objects are very limited. Thus, for the first time, the new composition was obtained, in which a half of the  $\text{Nd}^{3+}$  ions were replaced by  $\text{Zn}^{2+}$  ions. Zinc ions are

significantly smaller than  $\text{Nd}^{3+}$  and  $\text{La}^{3+}$  ions, which should have a positive effect on the proportion of proton transport; zinc is also an acceptor dopant, which generally increases the ionic conductivity. Finally, its introduction can also increase the density of the resulting ceramics [27].

## 2. Results and Discussion

### 2.1. Structure Characterization

All synthesized samples  $\text{La}_2\text{ZnNdO}_{5.5}$ ,  $\text{La}_2\text{Nd}_{0.9}\text{Ca}_{0.1}\text{ZnO}_{5.45}$ , and  $\text{La}_2\text{ZnNd}_{0.9}\text{Ca}_{0.1}\text{O}_{5.45}$  were found to be single-phase at room temperature, as an example the results of Rietveld refinement patterns are shown for the  $\text{La}_2\text{ZnNdO}_{5.5}$  sample (Figure 1). The phase of  $\text{La}_2\text{ZnNdO}_{5.5}$  and Ca-doped samples crystallized in a trigonal symmetry (s.g.  $P3m1$ ). These oxides are isostructural with  $\text{La}_2\text{O}_3$  as well as  $\text{LaNdO}_3$ . No superstructure lines were found in the diffraction patterns, which implies that no ordering of the cations occurred during doping, i.e., zinc and calcium are statistically distributed in the  $\text{LaNdO}_3$ . It should also be noted that in this work, the process of calcium doping was controlled by the creation of an initial deficiency of lanthanum or neodymium.

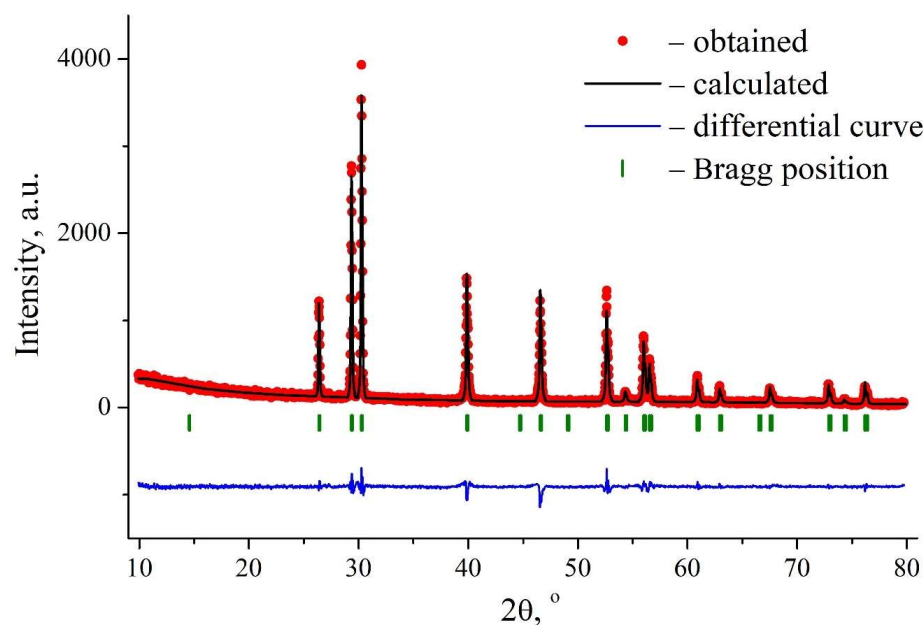


**Figure 1.** X-ray diffraction pattern of  $\text{La}_2\text{ZnNdO}_{5.5}$ ; observed (points), calculated (line), difference data (bottom), and angular positions of reflections (dashes) are shown.

The unit cell refinement parameters are given in Table 1.

**Table 1.** Refined lattice parameters of  $\text{La}_2\text{ZnNdO}_{5.5}$  and Ca-doped solid solutions.

Compositions	a (Å)	c (Å)	V (Å <sup>3</sup> )
$\text{La}_2\text{ZnNdO}_{5.5}$	3.906 (6)	6.091 (8)	80.51 (451)
$\text{La}_{1.9}\text{Ca}_{0.1}\text{ZnNdO}_{5.45}$	3.895 (3)	6.075 (6)	79.83 (653)
$\text{La}_2\text{ZnNd}_{0.9}\text{Ca}_{0.1}\text{O}_{5.45}$	3.897 (4)	6.081 (4)	79.99 (893)

Lattice parameters are not strongly affected by calcium doping. The changes in the lattice parameters are the result of the action of two parameters: first, the ratio of the radii of the doping and native ions, and, second, the presence of oxygen vacancies (the appearance of oxygen vacancies leads to a decrease in the cell parameters as well [28]).

Thus, on the one hand, the introduction of calcium ions into the lattice leads to the creation of oxygen vacancies in the system, which causes a reduction in the lattice parameters, according to the equations:



On the other hand, the sizes of the cations are close, but some differences correspond to the following order:  $r_{\text{La}} = 1.1 \text{ \AA} > r_{\text{Ca}} = 1.06 \text{ \AA} > r_{\text{Nd}} = 1.046 \text{ \AA}$  [29]. Thus, in the case of  $\text{La}_2\text{ZnNd}_{0.9}\text{Ca}_{0.1}\text{O}_{5.45}$ , the decrease is due to the appearance of vacancies, but in the case of  $\text{La}_{1.9}\text{Ca}_{0.1}\text{ZnNdO}_{5.45}$ , it is the sum of both factors and the decrease in volume is more significant.

The SEM images for the powder samples are given in Figure 2. The results show that the grain size was in a range of  $\sim 2 \mu\text{m}$ ; grain boundaries were clean. Introduction of calcium does not affect the morphology of the samples.

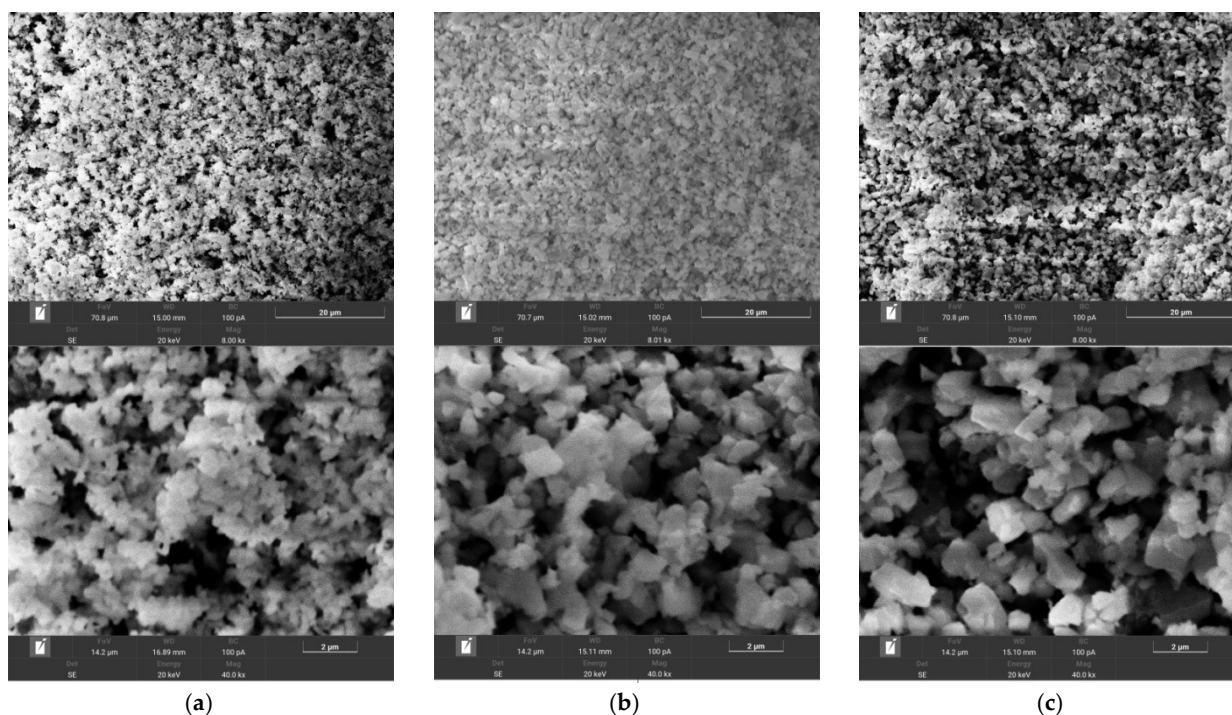


Figure 2. SEM images of  $\text{La}_2\text{ZnNdO}_{5.5}$  (a),  $\text{La}_{1.9}\text{Ca}_{0.1}\text{ZnNdO}_{5.45}$  (b), and  $\text{La}_2\text{ZnNd}_{0.9}\text{Ca}_{0.1}\text{O}_{5.45}$  (c) powders.

Figure 3 shows EDS maps for the elements of the  $\text{La}_{1.9}\text{Ca}_{0.1}\text{ZnNdO}_{5.45}$ ; the homogeneous distribution of elements is clearly visible, and there are no impurities. The cationic composition is in good agreement with the theoretical values (Table 2).

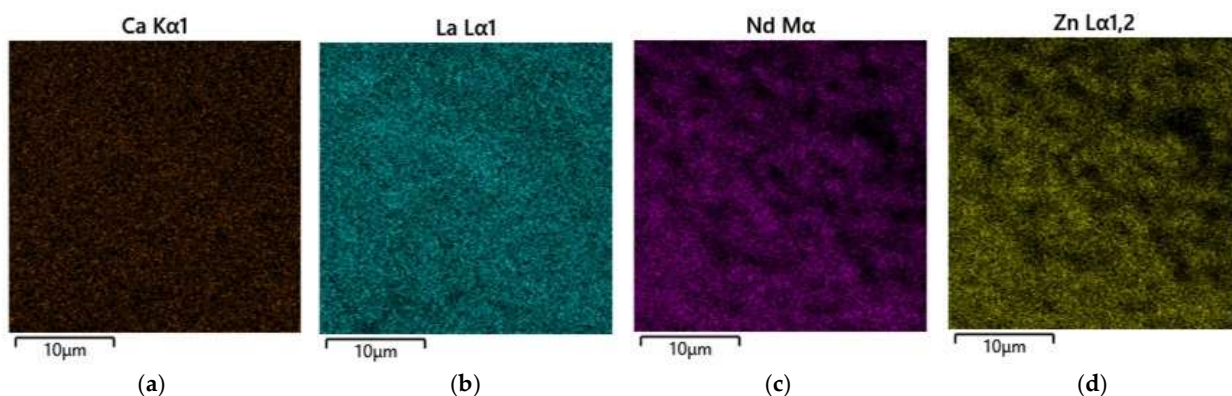


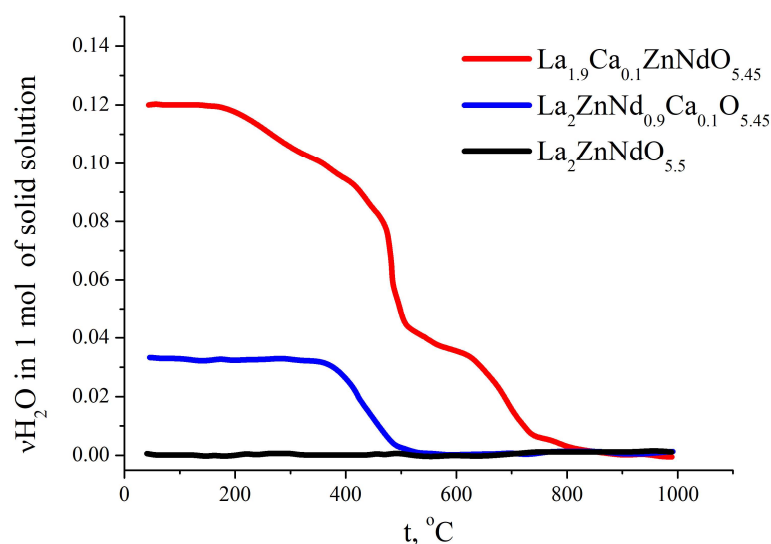
Figure 3. EDS maps of CaLZN for calcium (a), lanthanum (b), neodymium (c), and zinc (d).

**Table 2.** The average element ratios determined by EDS analysis for the sample  $La_{1.9}Ca_{0.1}ZnNdO_{5.45}$  (theoretical values are in brackets).

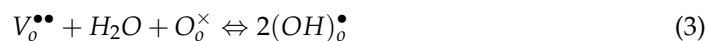
Element	Ca	La	Nd	Zn
Content, atomic %	2.2 (2.5)	48.1 (47.5)	25.5 (25.0)	24.2 (25.0)

## 2.2. Hydration Properties

During the TG studies, the possibility of interaction of the samples with water vapor was revealed. These data are shown in Figure 4.  $La_2ZnNdO_{5.5}$  does not interact with water vapor; therefore, it can be assumed that oxygen vacancies in this oxide are not available for water incorporation. This may be due to the tendency of zinc to form stable low-coordination polyhedra, which do not tend to transform into polyhedra with a higher coordination number.

**Figure 4.** TG data for  $La_2ZnNdO_{5.5}$ ,  $La_{1.9}Ca_{0.1}ZnNdO_{5.45}$  and  $La_2ZnNd_{0.9}Ca_{0.1}O_{5.45}$  samples.

Oppositely, the Ca-containing samples  $La_{1.9}Ca_{0.1}ZnNdO_{5.45}$  and  $La_2ZnNd_{0.9}Ca_{0.1}O_{5.45}$  are able to incorporate up to 0.12 and 0.035 mol  $H_2O$  in the structure, respectively. The interaction of water with the oxygen vacancies created by the introduction of calcium (Equations (1) and (2)) can be described by the following reaction:

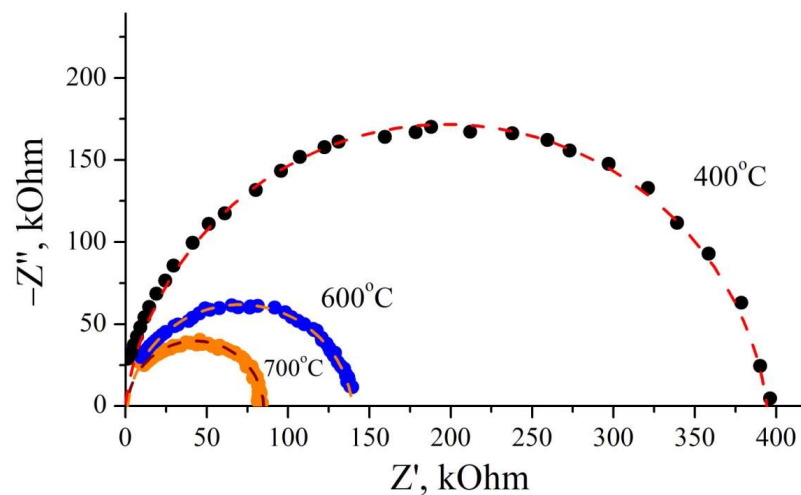


where  $V_o^{\bullet\bullet}$  is the oxygen vacancy,  $O_o^{\times}$  is the oxygen atom in a regular position, and  $(OH)_o^{\bullet}$  is the hydroxyl group in the oxygen sublattice. However, it should be noted that the sample with a smaller lattice volume is able to retain a greater amount of water. A redistribution of cations with different coordination numbers may be responsible for this effect.

## 2.3. Conductivity Properties

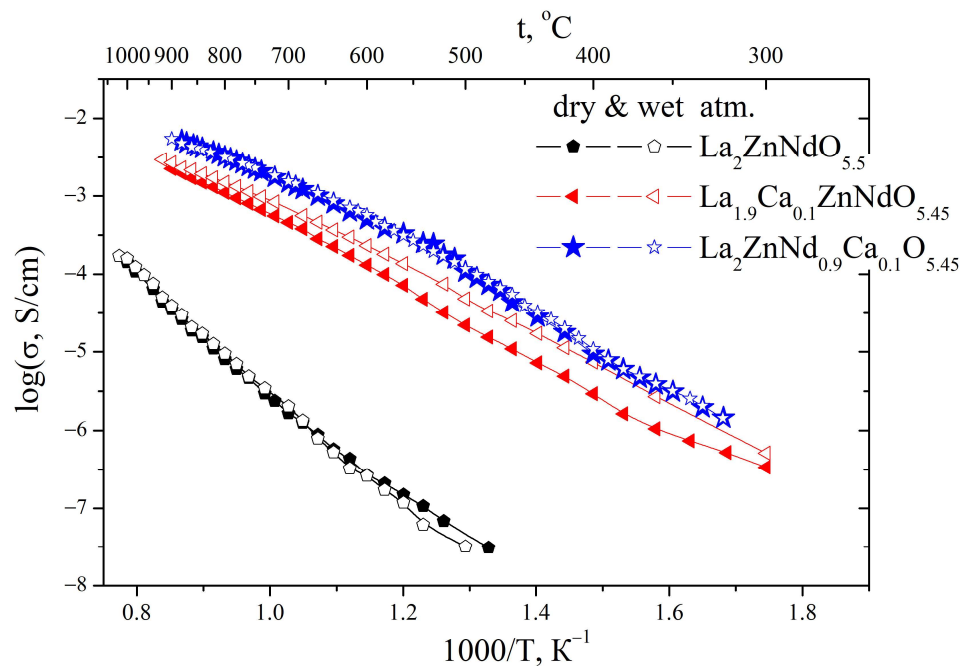
### 2.3.1. Conductivity Measurements as a Function of Temperature

Figure 5 shows typical complex impedance plots at different temperatures. A semicircle starting from zero of the complex impedance plot was observed over the entire temperature range investigated. This semicircle was associated with the bulk process as the value of the capacitance was in the range of  $10^{-11}$ – $10^{-10}$  F (which is typical for bulk processes).



**Figure 5.** The impedance spectra of  $La_2ZnNdO_{5.5}$  recorded at 400–700 °C.

The temperature dependencies of the conductivities for the  $La_2ZnNdO_{5.5}$  compound and doped samples of  $La_{1.9}Ca_{0.1}ZnNdO_{5.45}$  and  $La_2ZnNd_{0.9}Ca_{0.1}O_{5.45}$  are shown in Figure 6.



**Figure 6.** Temperature dependencies of the conductivities of  $La_2ZnNdO_{5.5}$ ,  $La_{1.9}Ca_{0.1}ZnNdO_{5.45}$ , and  $La_2ZnNd_{0.9}Ca_{0.1}O_{5.4}$ .

Calcium doping leads to an increase in total conductivity of more than two orders of magnitude over the investigated temperature range. To explain this, let us look at the factors that influence ionic conductivity [30,31]. There are two main factors—mobility  $\mu_i$  and concentration  $C_i$ . These are related to conductivity by the equation:

$$\sigma = Z_i e \mu_i C_i. \quad (4)$$

At introduction of calcium in  $La_2ZnNdO_{5.5}$  increases the concentration of oxygen vacancies in the structure (Equations (1) and (2)); this explains the increase in conductivity. If we compare the conductivity of calcium-substituted samples with each other, the phase with larger lattice volume  $La_2ZnNd_{0.9}Ca_{0.1}O_{5.45}$  exhibits the highest conductivity. This agrees with the provisions of Sammells' work [30] that the larger the lattice volume, the higher the

mobility of the ions and, hence, the conductivity, which is also accompanied by a decrease in the activation energy. The activation energies for  $La_2ZnNdO_{5.5}$ ,  $La_{1.9}Ca_{0.1}ZnNdO_{5.45}$ , and  $La_2ZnNd_{0.9}Ca_{0.1}O_{5.45}$  were 1.59, 0.79, and 0.68 eV, respectively, indicating a facilitation of the transport process.

A comparison of conductivity in a dry and humid atmosphere is shown in Figure 6. The response to the changes in humidity correlates with the water uptake data. The  $La_2ZnNdO_{5.5}$  and  $La_2ZnNd_{0.9}Ca_{0.1}O_{5.45}$  samples showed little response to changes in humidity.

At the same time, for the  $La_{1.9}Ca_{0.1}ZnNdO_{5.45}$  sample, the influence of humidity begins to be demonstrated at temperatures below 900 °C (which is consistent with the TG data), manifesting itself in an increase in the total conductivity. This is explained by the fact that, during hydration according to Equation (3), mobile proton defects are formed, which contribute additionally to charge transfer.

To confirm the assumptions about the nature of the conductivity, the electrical conductivity of the samples was studied as a function of oxygen partial pressure ( $pO_2$ ).

### 2.3.2. Conductivity Measurements as a Function of Oxygen Partial Pressure

Figures 7 and 8 show the results of the conductivity measurements as a function of  $pO_2$  in the temperature range of 500–900 °C. Two regions can be distinguished on these isotherms: a region of electrolytic conductivity as a plateau and a region at high oxygen partial pressures where a positive slope of the dependence is observed. For  $pO_2 < 10^{-4}$  atm, the concentration of oxygen vacancies is fixed by the doping level, and a  $pO_2$ -independent oxygen-ionic conductivity can be observed. The incorporation of oxygen into the lattice with increasing  $pO_2$  is accompanied by the generation of electron holes ( $h^\bullet$ ), which can be described as follows:

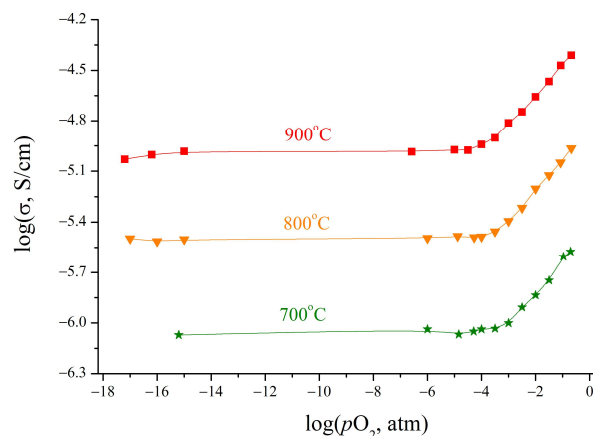


**Figure 7.** Conductivity as a function of oxygen partial pressure at different temperatures in dry atmosphere for  $La_2ZnNdO_{5.5}$  sample.

Therefore, it can be assumed that  $La_2ZnNdO_{5.5}$  and Ca-doped samples are mixed oxygen-hole conductors in a dry atmosphere. Oxygen-ion transference numbers were calculated as a ratio of ionic conductivity to total conductivity:

$$t_{ion} = \sigma_{ion} / \sigma_{total} \quad (6)$$

For the undoped sample, the isotherms could be obtained in the temperature range of 700–900 °C due to the low conductivity values (Figure 7). The  $La_2ZnNdO_{5.5}$  sample has the lowest  $t_{ion}$  levels, ~30%; however, the proportion of the ion contribution increases with decreasing temperature. In contrast to  $La_2ZnNdO_{5.5}$ , the Ca-substituted samples have stable transference numbers of ~40% throughout the study interval (Figure 9). This increase may be due to an increase in the number of oxygen vacancies upon the introduction of calcium, as it acts as an acceptor dopant.

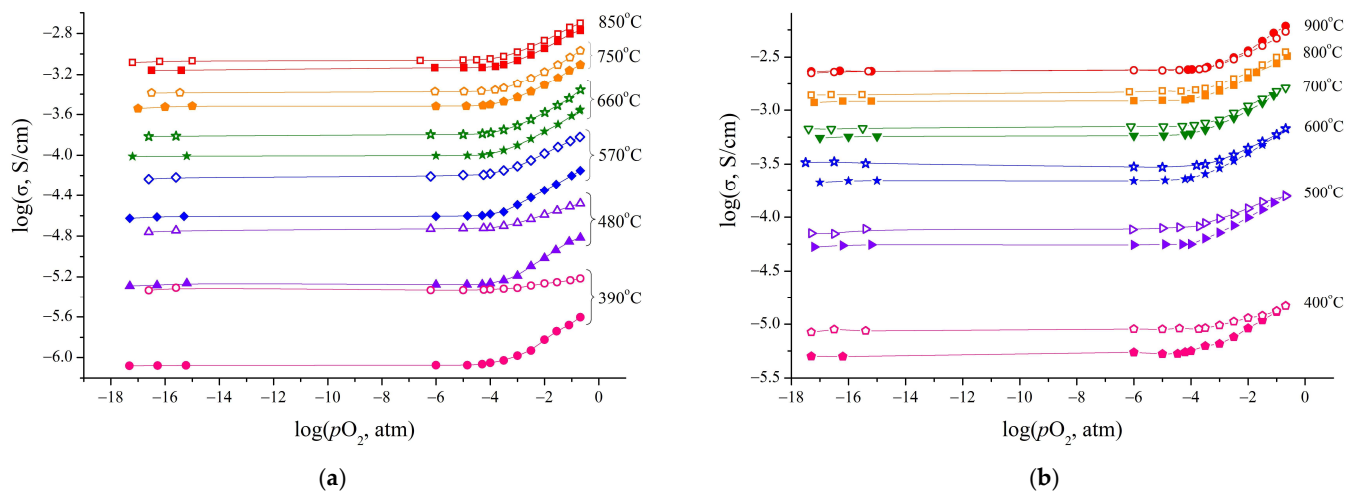


**Figure 8.** Conductivity of  $La_{1.9}Ca_{0.1}ZnNdO_{5.45}$  (a) and  $La_2ZnNd_{0.9}Ca_{0.1}O_{5.45}$  (b) samples as a function of  $pO_2$  at different temperatures.

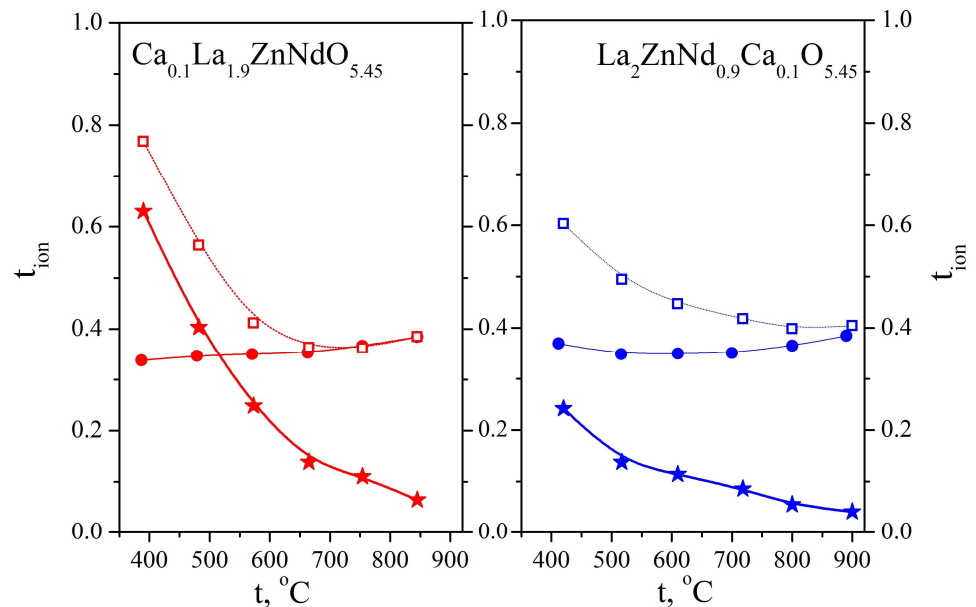
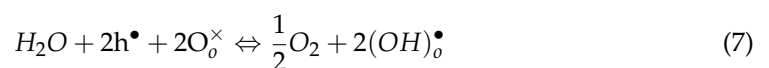


**Figure 9.** Calculated transport numbers: total ionic in humid air (squares), total ionic in dry air or oxygen-ion (circles) and proton (stars) for  $La_{1.9}Ca_{0.1}ZnNdO_{5.45}$  (red) and  $La_2ZnNd_{0.9}Ca_{0.1}O_{5.45}$  (blue).

In a humid atmosphere below 900 °C for the calcium-substituted samples, an increase in conductivity in the electrolytic region coupled with a slight expansion of the plateau region are observed (Figure 8). This is due to an increase in the ionic component of the conductivity due to the appearance of more mobile proton charge carriers. However, the form of the dependence is different for  $La_{1.9}Ca_{0.1}ZnNdO_{5.45}$  and  $La_2ZnNd_{0.9}Ca_{0.1}O_{5.45}$ . The effect of humidity on  $La_{1.9}Ca_{0.1}ZnNdO_{5.45}$  being significantly greater than that on  $La_2ZnNd_{0.9}Ca_{0.1}O_{5.45}$ , and in the region of high oxygen pressures,  $La_2ZnNd_{0.9}Ca_{0.1}O_{5.45}$  is characterized by an equal conductivity value for wet and dry atmospheres (as we can see in Figure 6), which is related to the smaller contribution of proton carriers to the conductivity of this sample.

The formation of proton defects can occur due to interaction with electron carriers according to the equation:



Therefore, for  $La_2ZnNd_{0.9}Ca_{0.1}O_{5.45}$  with a high proportion of electronic conductivity in a humid atmosphere, the concentration of hole carriers, which are more mobile than protons, decreases, reducing the overall conductivity; however, this can be compensated by an increase in the proton contribution, which tends to increase significantly with decreasing temperature. Thus, we observe the opposite effect of these two factors.

The values of the ion transport numbers in a humid atmosphere increase with decreasing temperature (Figure 9), approaching 0.8 for  $La_{1.9}Ca_{0.1}ZnNdO_{5.45}$  and 0.6 for  $La_2ZnNd_{0.9}Ca_{0.1}O_{5.45}$ , which is associated with an increase in the proton concentration at low temperatures (see TG data).

Using expression (6), the proton transport numbers were also calculated. According to the data presented in Figure 9, the ratio of the contributions of the ionic conductivity in the calcium-substituted samples is significantly different.  $La_{1.9}Ca_{0.1}ZnNdO_{5.45}$  is characterized by a significant increase in the proton component, and, at temperatures below 650 °C, proton transport dominates over oxygen-ion transport. However, for the sample  $La_2ZnNd_{0.9}Ca_{0.1}O_{5.45}$ , despite some increase in proton transport with decreasing temperature, associated with an increase in proton concentration, the predominant type of transport remains oxygen-ion transport throughout the temperature range investigated. These correspond to the dependence discovered by Norby [26], in which the level of proton conductivity increases with decreasing cation size and denser lattice packing. For the compositions of  $La_{1.9}Ca_{0.1}ZnNdO_{5.45}$  and  $La_2ZnNd_{0.9}Ca_{0.1}O_{5.45}$ , the conductivity was separated and the partial contribution changes with temperature were analyzed (Figure 10). Such a separation was based on the assumption that the value of the oxygen-ion transport is independent of humidity.

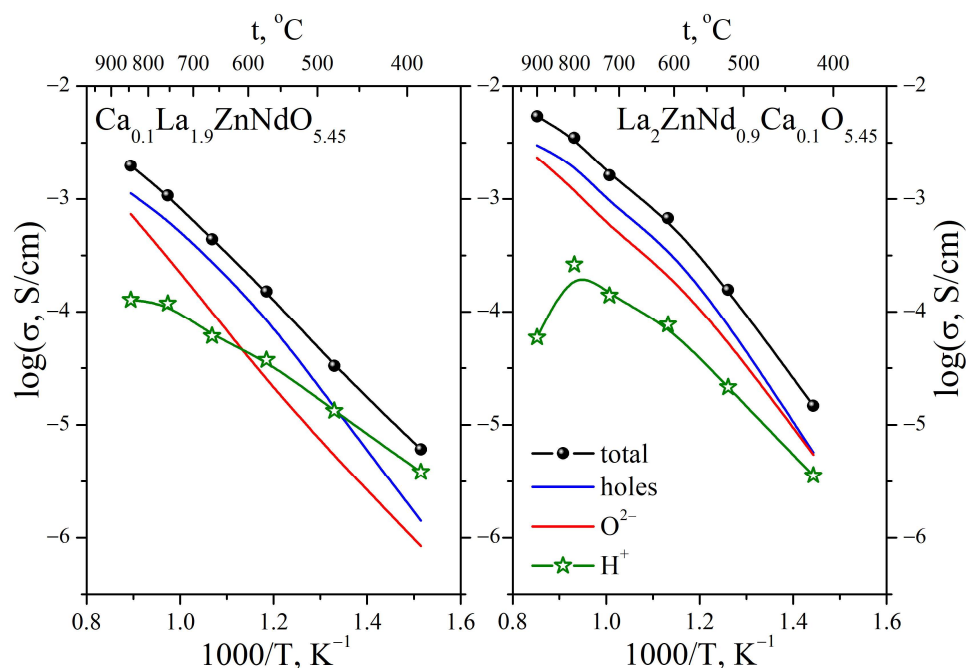


**Figure 10.** Temperature dependencies of partial conductivities for  $La_{1.9}Ca_{0.1}ZnNdO_{5.45}$  and  $La_2ZnNd_{0.9}Ca_{0.1}O_{5.45}$  samples.

For the  $La_{1.9}Ca_{0.1}ZnNdO_{5.45}$  sample below 500 °C, the total conductivity is attributed mainly to proton transport, which is not observed for the  $La_2ZnNd_{0.9}Ca_{0.1}O_{5.45}$  sample. The  $La_2ZnNd_{0.9}Ca_{0.1}O_{5.45}$  sample becomes predominantly an ionic conductor only at temperatures below 500 °C in a humid atmosphere, but the dominant type of transport cannot be distinguished.

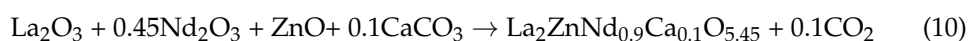
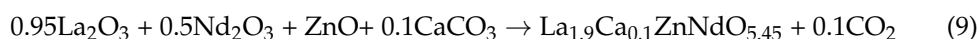
It is important to note that no hydrolysis decomposition of the phases was observed in these experimental conditions (temperature range 300–1000 °C and  $p_{H_2O} = 2 \times 10^{-2}$  atm),

i.e., the samples are stable under the specified conditions. The possibility of proton transfer dominating was also confirmed. In addition, the phases are chemically stable in a wide range of  $pO_2$ . Thus, the phases under further modification are promising as electrolytes for electrochemical devices.

### 3. Materials and Methods

#### 3.1. Synthesis of Perovskite $La_2NdZnO_{5.5}$ and Doped Samples

The  $La_2NdZnO_{5.5}$  phase and Ca-doped samples were synthesized by the solid-state method. High-purity powders (99.99% purity, REACHIM, Moscow, Russian Federation) of  $Nd_2O_3$ ,  $La_2O_3$ , and  $CaCO_3$  were used as precursors. They were pre-calcined before weighing:  $Nd_2O_3$  at 500 °C,  $CaCO_3$  at 300 °C for 5 h to remove adsorption water;  $La_2O_3$  was calcined at 1100 °C for 3 h to decompose the surface lanthanum carbonates  $LaOHCO_3$  and  $La_2O_2CO_3$  [32]. Stoichiometric amounts of oxides were weighed on an analytical balance (Sartorius AG, Göttingen, Germany) with an accuracy of  $\pm 0.0001$  g, and then mixed with ethanol and manually ground in an agate mortar and calcined in the temperature range of 700–1400 °C with heating steps of 100 °C; isothermal holding for 24 h and cooling in the furnace; and intermediate grinding was performed for each step. The solid-phase reactions were carried out according to the following equations:



#### 3.2. X-ray Diffraction

The phase composition was monitored by powder X-ray diffraction (XRD) on a D8 Advance diffractometer (Bruker, Billerica, MA, USA) using  $Cu\ K\alpha$  radiation in a  $2\theta$  range of  $10^\circ$ – $80^\circ$  with a step of  $0.05^\circ$  and an exposure time of 1 s, a voltage of 40 kV, and a current of 40 mA. The basic cell parameters of the samples were determined by Rietveld refinement using the FULLPROF software [33]. Phases have been identified according to the Inorganic Crystal Structure Database (ICSD, version 2020/2).

#### 3.3. Thermogravimetric Analysis

Thermogravimetric analysis (TGA) was used to determine the proton concentrations. The TGA was performed on the hydrated powder samples using a STA 409 PC analyzer (Netzsch, Selb, Germany). The samples were first treated at 1000 °C for 1 h in dry Ar to remove any volatiles ( $CO_2$ ,  $H_2O$ ), and then the samples were cooled to 200 °C at a rate of 1 °C/min in humid air ( $pH_2O = 2 \times 10^{-2}$  atm) from which the  $CO_2$  was removed. The samples were then hermetically sealed.

#### 3.4. Conductivity Measurements

Preparation of compacted samples. For electrical measurements, the powder samples were compacted to pellets at 50 MPa on a PLG-12 laboratory hydraulic press (LabTools, Saint-Petersburg, Russia). The solution of rubber in hexane was used as a plasticizer. The pellets were sintered at 1300 °C for 24 h. The values of relative densities were found to be ~95–97%. The polished surfaces of the sintered pellets were then coated with Pt paste and annealed at 900 °C for 3 h in air.

Measurement conditions. Conductivity measurements as a function of temperature were carried out in the temperature range of 200–1000 °C with a cooling rate of 1 °C/min and taken every 20 °C. The AC conductivity of the samples was measured using the 2-probe method with the impedance spectrometer Z-1000P (Electrochemical Instruments (Elins), Chernogolovka, Russia) in the frequency range 1– $10^6$  Hz. The bulk resistance was calculated from a complex impedance plot using Zview software fitting (Scribner Associates, Southern Pines, NC, USA) [34].

Conductivity measurements as a function of oxygen partial pressure ( $pO_2$ ) were made using the direct-current 2-probe method in the temperature range 400–900 °C and taken every 100 °C at oxygen partial pressure ( $pO_2$ ) ranging from 0.21 to  $10^{-18}$  atm. Each  $pO_2$  step was held for 4 h to allow the sample to equilibrate with a gas phase. Measurements were performed using a coupled electrochemical pump and an YSZ sensor, controlled by a Zirconia-M (Project Zirconia, Ekaterinburg, Russia [35]). This automatic microprocessor controller was used to adjust the temperature and oxygen partial pressure within the electrochemical cell. The relative errors in the determination of the conductivity values did not exceed 5% and were caused mainly by the accuracy of the measurement of the dimensional parameters of the sample.

The temperature inside the furnace was controlled with an accuracy of  $\pm 1$  °C by means of a Pt-Pt/Rh thermocouple placed next to the ceramic sample.

Conductivity measurements were carried out in dry and wet atmospheres.

Preparation of “dry” and “wet” air. To produce the desired humidity and to remove  $CO_2$ , the air was then bubbled through 30% NaOH and saturated KBr solutions at room temperature to produce “wet” air. To obtain a “dry” atmosphere, the air was passed through NaOH and  $P_2O_5$  powders. Partial water vapor pressure was measured with a humidity sensor HIH-3610 (Honeywell, Freeport, IL, USA) and was  $2 \times 10^{-2}$  atm for “wet” and  $3.5 \times 10^{-5}$  atm for “dry” air.

#### 4. Conclusions

$La_2ZnNdO_{5.5}$  oxide and calcium-substituted derivatives were synthesized for the first time. The electrical properties of the phases, as well as the possibility of interaction with water vapor, have been under investigation. The introduction of calcium significantly increases the electrical conductivity by more than two orders of magnitude, but the degree of increase depends on which initial ion is substituted. Sample  $La_2ZnNd_{0.9}Ca_{0.1}O_{5.45}$  has the highest electrical conductivity of about  $10^{-3}$  S·cm $^{-1}$  at 650 °C. It is shown that by varying the average radius of the cation (i.e., by introducing a larger or smaller ion into the native lattice), one can influence the ratio of the contributions to ionic conductivity (proton and oxygen-ion). Substitution of lanthanum by a smaller calcium ion reduces the lattice volume and increases the proportion of proton transport to values where it becomes the dominant type of transport ( $T > 500$  °C). At the same time, substitution of niobium by a larger calcium ion increases the lattice volume and the proportion of oxygen ion transport. These data are fully consistent with Norby’s suggestion that oxides with denser lattice packing favor proton transport over oxygen-ion transport [26].

**Author Contributions:** Conceptualization, K.B. and I.A.; methodology, K.B. and I.A.; investigation, S.P., A.E., K.B. and D.M.; data curation, K.B.; writing—original draft preparation, K.B.; writing—review and editing, K.B. and D.M.; visualization, K.B. and D.M. All authors have read and agreed to the published version of the manuscript.

**Funding:** The research funding from the Ministry of Science and Higher Education of the Russian Federation (Ural Federal University Program of Development within the Priority-2030 Program) is gratefully acknowledged.

**Data Availability Statement:** The data presented in this study are available on request from the corresponding author.

**Conflicts of Interest:** The authors declare no conflict of interest.

#### References

1. Kim, D.; Bae, K.T.; Kim, K.J.; Im, H.-N.; Jang, S.; Oh, S.; Lee, S.W.; Shin, T.H.; Lee, K.T. High-performance protonic ceramic electrochemical cells. *ACS Energy Lett.* **2022**, *7*, 2393–2400. [[CrossRef](#)]
2. Liu, F.; Ding, D.; Duan, C. Protonic ceramic electrochemical cells for synthesizing sustainable chemicals and fuels. *Adv. Sci.* **2023**, *2023*, 2206478. [[CrossRef](#)]
3. Tian, H.; Luo, Z.; Song, Y.; Zhou, Y.; Gong, M.; Li, W.; Shao, Z.; Liu, M.; Liu, X. Protonic ceramic materials for clean and sustainable energy: Advantages and challenges. *Int. Mater. Rev.* **2022**, *2022*, 1–29. [[CrossRef](#)]

4. Corigliano, O.; Pagnotta, L.; Fragiaco, P. On the technology of solid oxide fuel cell (SOFC) energy systems for stationary power generation: A review. *Sustainability* **2022**, *14*, 15276. [[CrossRef](#)]
5. Zvonareva, I.; Fu, X.-Z.; Medvedev, D.; Shao, Z. Electrochemistry and energy conversion features of protonic ceramic cells with mixed ionic-electronic electrolytes. *Energy Environ. Sci.* **2022**, *15*, 439–465. [[CrossRef](#)]
6. Zhang, W.; Hu, Y.H. Progress in proton-conducting oxides as electrolytes for low-temperature solid oxide fuel cells: From materials to devices. *Energy Sci. Eng.* **2021**, *9*, 984–1011. [[CrossRef](#)]
7. Guo, R.; He, T. High-entropy perovskite electrolyte for protonic ceramic fuel cells operating below 600 °C. *ACS Mater. Lett.* **2022**, *4*, 1646–1652. [[CrossRef](#)]
8. Wang, C.; Li, Z.; Zhao, S.; Xia, L.; Zhu, M.; Han, M.; Ni, M. Modelling of an integrated protonic ceramic electrolyzer cell (PCEC) for methanol synthesis. *J. Power Sources* **2023**, *559*, 232667. [[CrossRef](#)]
9. Ji, H.I.; Lee, J.H.; Son, J.W.; Yoon, K.J.; Yang, S.; Kim, B.K. Protonic ceramic electrolysis cells for fuel production: A brief review. *J. Korean Ceram. Soc.* **2020**, *57*, 480–494. [[CrossRef](#)]
10. Tarasova, N. Layered perovskites  $BaLn_nIn_nO_{3n+1}$  ( $n = 1, 2$ ) for electrochemical applications: A mini review. *Membranes* **2023**, *13*, 34. [[CrossRef](#)]
11. Arsad, A.Z.; Hannan, M.A.; Al-Shetwi, A.Q.; Mansur, M.; Muttaqi, K.M.; Dong, Z.Y.; Blaabjerg, F. Hydrogen energy storage integrated hybrid renewable energy systems: A review analysis for future research directions. *Int. J. Hydrogen Energy* **2022**, *47*, 17285–17312. [[CrossRef](#)]
12. Kumar, S.S.; Lim, H. An overview of water electrolysis technologies for green hydrogen production. *Energy Rep.* **2022**, *8*, 13793–13813. [[CrossRef](#)]
13. Huang, L.; Huang, X.; Yan, J.; Liu, Y.; Jiang, H.; Zhang, H.; Tang, J.; Liu, Q. Research progresses on the application of perovskite in adsorption and photocatalytic removal of water pollutants. *J. Hazard. Mater.* **2023**, *442*, 130024. [[CrossRef](#)]
14. Scovell, M.D. Explaining hydrogen energy technology acceptance: A critical review. *Int. J. Hydrogen Energy* **2022**, *47*, 10441–10459. [[CrossRef](#)]
15. Buonomano, A.; Barone, G.; Forzano, C. Advanced energy technologies, methods, and policies to support the sustainable development of energy, water and environment systems. *Energy Rep.* **2022**, *8*, 4844–4853. [[CrossRef](#)]
16. Syafkeena, M.A.N.; Zainor, M.L.; Hassan, O.H.; Baharuddin, N.A.; Othman, M.H.D.; Tseng, C.-J.; Osman, N. Review on the preparation of electrolyte thin films based on cerate-zirconate oxides for electrochemical analysis of anode-supported proton ceramic fuel cells. *J. Alloys Compd.* **2022**, *918*, 165434. [[CrossRef](#)]
17. Rasaki, S.A.; Liu, C.; Lao, C. A review of current performance of rare earth metal-doped barium zirconate perovskite: The promising electrode and electrolyte material for the protonic ceramic fuel cells. *Prog. Solid State Chem.* **2021**, *63*, 100325. [[CrossRef](#)]
18. Qiao, Z.; Li, S.; Li, Y.; Xu, N.; Xiang, K. Structure, mechanical properties, and thermal conductivity of  $BaZrO_3$  doped at the A-B site. *Ceram. Int.* **2022**, *48*, 12529–12536. [[CrossRef](#)]
19. Guo, R.; Li, D.; Guan, R.; Kong, D.; Cui, Z.; Zhou, Z.; He, T. Sn–Dy–Cu triply doped  $BaZr_{0.1}Ce_{0.7}Y_{0.2}O_{3-\delta}$ : A chemically stable and highly proton-conductive electrolyte for low-temperature solid oxide fuel cells. *ACS Sustain. Chem. Eng.* **2022**, *10*, 5352–5362. [[CrossRef](#)]
20. Nayak, A.K.; Sasmal, A. Recent advance on fundamental properties and synthesis of barium zirconate for proton conducting ceramic fuel cell. *J. Clean. Prod.* **2023**, *386*, 135827. [[CrossRef](#)]
21. Norby, T.; Dyrllie, O.; Kofstad, P. Protonic conduction in acceptor-doped cubic rare-earth sesquioxides. *J. Am. Ceram. Soc.* **1992**, *75*, 1176–1181. [[CrossRef](#)]
22. Larring, Y.; Norby, T. Protons in rare-earth oxides. *Solid State Ion.* **1995**, *77*, 147–151. [[CrossRef](#)]
23. Larring, Y.; Norby, T. The equilibrium between water vapor, protons, and oxygen vacancies in rare earth oxides. *Solid State Ion.* **1997**, *97*, 523–528. [[CrossRef](#)]
24. Haugsrud, R.; Larring, Y.; Norby, T. Proton conductivity of Ca-doped  $Tb_2O_3$ . *Solid State Ion.* **2005**, *176*, 2957–2961. [[CrossRef](#)]
25. Norby, T.; Wideroe, M.; Glockner, R.; Larring, Y. Hydrogen in oxides. *Dalton Trans.* **2004**, *19*, 3015. [[CrossRef](#)]
26. Norby, T.; Oddvar, D.; Kofstad, P. Protons in Ca-doped  $La_2O_3$ ,  $Nd_2O_3$  and  $LaNdO_3$ . *Solid State Ion.* **1992**, *53–56*, 446–452. [[CrossRef](#)]
27. Kuzmin, A.V.; Lesnichyova, A.S.; Tropin, E.S.; Stroeva, A.Y.; Vorotnikov, V.A.; Solodyankina, D.M.; Belyakov, S.A.; Plekhanov, M.S.; Farlenkov, A.S.; Osinkin, D.A.; et al.  $LaScO_3$ -based electrolyte for protonic ceramic fuel cells: Influence of sintering additives on the transport properties and electrochemical performance. *J. Power Sources* **2020**, *466*, 228255. [[CrossRef](#)]
28. Chatzichristodoulou, C.; Norby, P.; Hendriksen, P.V.; Mogensen, M.B. Size of oxide vacancies in fluorite and perovskite structured oxides. *J. Electroceram.* **2015**, *34*, 100–107. [[CrossRef](#)]
29. Shannon, R.D. Revised effective ionic radii and systematic studies of interatomic distances in halides and chalcogenides. *Acta Crystallogr. Sect. A Found. Crystallogr.* **1976**, *32*, 751–767. [[CrossRef](#)]
30. Sammells, A.F.; Cook, R.L.; White, J.H.; Osborne, J.J.; MacDuff, R.C. Rational selection of advanced solid electrolytes for intermediate temperature fuel cells. *Solid State Ion.* **1992**, *52*, 111–123. [[CrossRef](#)]
31. Richter, J.; Holtappels, P.; Graule, T.; Nakamura, T.; Gauckler, L.J. Materials design for perovskite SOFC cathodes. *Monatsh. Chem.* **2009**, *140*, 985–999. [[CrossRef](#)]
32. Bakiz, B.; Guinneton, F.; Arab, M.; Benhachemi, A.; Villain, S.; Satre, P.; Gavarri, J.-R. Carbonatation and decarbonation kinetics in the  $La_2O_3$ - $La_2O_2CO_3$  system under  $CO_2$  gas flows. *Adv. Mater. Sci. Eng.* **2010**, *2010*, 360597. [[CrossRef](#)]

33. Rodríguez-Carvajal, J. Recent Developments of the Program FULLPROF In Commission on Powder Diffraction (IUCr). *Newsletter* **2001**, *26*, 12–19. Available online: <http://journals.iucr.org/iucr-top/comm/cpd/Newsletters/> (accessed on 10 March 2023).
34. Johnson, D. *ZView: A Software Program for IES Analysis, Version 2.8*; Scribner Associates: South Pines, NC, USA, 2002; p. 200.
35. Zirconia Project. Available online: <https://zirconiaproject.wordpress.com/devices/zirconiam/> (accessed on 2 April 2023).

**Disclaimer/Publisher's Note:** The statements, opinions and data contained in all publications are solely those of the individual author(s) and contributor(s) and not of MDPI and/or the editor(s). MDPI and/or the editor(s) disclaim responsibility for any injury to people or property resulting from any ideas, methods, instructions or products referred to in the content.